High-sensitivity magnetometry with a single atom in a superposition of two circular Rydberg states

E. Dietsche, A. Larrouy, S. Haroche, J. Raimond, Michel Brune, S. Gleyzes

High-sensitivity magnetometry with a single atom in a superposition of two circular Rydberg states

E.K. Dietsche,[1] A. Larrouy,[1] S. Haroche,[1] J.M. Raimond,[1] M. Brune,[1] and S. Gleyzes[1]

[1] *Laboratoire Kastler Brossel, Collège de France, CNRS, ENS-Université PSL, Sorbonne Université, 11, place Marcelin Berthelot, 75005 Paris, France**

(Dated: December 13, 2023)

Superpositions of states with macroscopicallydifferent properties, named 'cats' after Schrödinger's Gedanken experiment, are extraordinarily sensitive probes of their environment. They can be used to investigate the decoherence mechanism and the quantum-to-classical transition [1–5] and to realize quantum-enabled sensors [6] with promising applications. We report here the creation of a "circular cat", namely an atom in a superposition of two circular Rydberg states with huge opposite magnetic momenta. It is is an exquisite probe of the magnetic field, able to perform a single-shot detection of a 13 nT field in only 20 μs. This single-atom cat is as sensitive as a set of 1800 ordinary atoms, demonstrating the usefulness of Rydberg state engineering for quantum-enabled technologies.

The precise measurement of magnetic fields has a large number of applications, from the monitoring of the brain activity to archaeology, from submarine detection to local mapping of fields in a nano-device [7–11]. The highest sensitivities are reached with SQUIDs [12] using macroscopic pickup coils or large atomic ensembles [13, 14], at the expense of detection volumes in the cm^3 range. A much higher spatial resolution, but a lesser sensitivity, is obtained with solid-state nano-devices [15] or with atoms [16–19], ions [20] or NV-center sensors [21], ultimately at the single-particle level as shown in pioneering experiments [22–25].

All the atom-like sensors so far are fundamentally limited by the magnetic moments of their ground states. They range from about one Bohr magneton (μ_B = 14 GHz/T) [24] to at most $10\,\mu_B$ for highly magnetic atoms such as Dysprosium [26]. Rydberg levels, with a high principal quantum number n, do not suffer from such a fundamental limitation. The circular states $|nC^{\pm}\rangle$, have an extremal magnetic moment, $\pm(n-1)\mu_B$ that can, in principle, be made arbitrarily large.

We report here the realization of a highly sensitive single-atom magnetometer based on Rydberg levels with $n \approx 50$. It relies on a quantum interference process involving a superposition of two circular states with opposite magnetic momenta, $|nC^+\rangle$ and $|nC^-\rangle$, prepared by quantum-state engineering in the Stark manifold of a Rubidium atom. In classical terms, this state corresponds to an electron orbiting in two opposite directions *at once* on a 0.3 μm diameter circular trajectory. By symmetry, these two states experience exactly the same Stark effect. This sensitive probe of magnetic fields is thus totally impervious to electrical perturbations, leading to a long coherence time for the superposition.

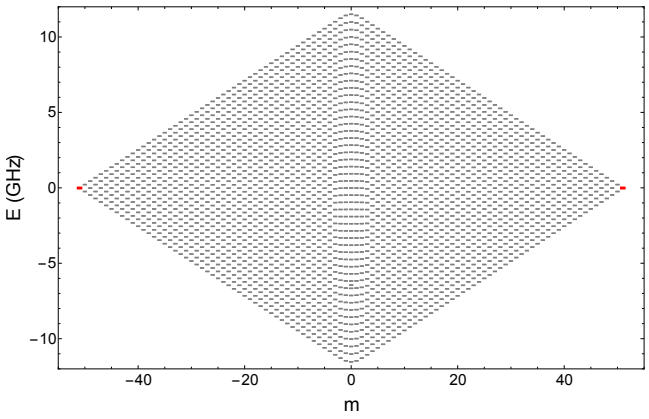

FIG. 1. **Stark manifold of the Rubidium atom.** All the energy levels in the $n = 52$ Stark manifold are represented versus the magnetic quantum number m in an electric field $F_0 = 2.30$ V/cm. The two circular states with opposite ms (red lines) are at the extremities of the lozenge structure. The regularity of the hydrogenic Stark pattern is broken for $|m| \leq 2$, revealing the influence of the quantum defects.

The $n = 52$ Rubidium Stark manifold is presented in Fig. 1 for an electric field $\mathbf{F}$ ($F = F_0 = 2.30$ V/cm) defining the quantization axis. The levels are sorted by values of the magnetic quantum number m, with $|m| < n$ (the electron spin is insensitive to the electromagnetic fields used to manipulate the atomic state and thus plays no role here). For $|m| > 2$, the electron orbits far from the ionic core and the structure is that of Hydrogen. The two circular states, with maximum $|m|$s, are at both extremities of the lozenge structure. At the first order in electric field, all states have equal spacings. The Stark transitions between two adjacent states in the m and $m \pm 1$ ladders have a frequency $\omega_s(n) = 3ea_0nF/2\hbar$ (a_0: Bohr radius), with $\omega_s(52) = 2\pi \times 230$ MHz for $F = F_0$. They can be selectively addressed by $\sigma^{\pm}$ circularly-polarized radiofrequency (rf) fields [27]. For $|m| \leq 2$, the levels depart notably from the hydrogenic structure, with non-vanishing quantum defects due to the finite core size.

The circular state $|52C^+\rangle$ can be prepared from the laser-accessible lower state in the $m = +2$ ladder ($|52; +2\rangle$) by a σ^+-polarized rf pulse at ω_s. The transfer

has a large efficiency and can be performed on a sub-μs time-scale [27]. Similarly, $|52C^-\rangle$ can be prepared from the lower $m = -2$ state ($|52;-2\rangle$) by a σ^- rf pulse. However, the two 'circularization' processes cannot be performed simultaneously nor sequentially: preparing $|52C^-\rangle$ transfers $|52C^+\rangle$ to low-m levels. We thus perform the 'positive' and 'negative' circularizations in different manifolds, the linear variation of ω_s with n making their independent manipulation possible.

The experiment takes place in a conducting structure sustaining the directing electric field $\mathbf{F}$ and the $\sigma^\pm$-polarized rf fields driving the Stark transitions. It is described in details in the Methods section. The sequence is schematized in Fig. 2(a). At $t = 0$, we excite with lasers about one atom in $|52;+2\rangle$ out of a thermal atomic beam. Between $t = 3.5$ μs and $t = 5.6$ μs, a succession of rf and mw pulses create a quantum superposition of $|52C^+\rangle$ and $|50C^-\rangle$. At $t = 5.9$ μs, a final mw pulse transfer $|50C^-\rangle$ to $|52C^-\rangle$ to prepare the desired circular state superposition (CSS), ideally $(|52C^+\rangle + |52C^-\rangle)/\sqrt{2}$.

The actual implementation of the sequence must take into account some limitations of the set-up. The $\sigma^\pm$ polarization purity is optimized at a fixed rf frequency. We use two fixed-frequency independent rf sources for σ^+ and σ^-, respectively resonant with $\omega_s(52)$ and $\omega_s(50)$ for $F = F_0$. We change F when needed to set the other rf transitions in the sequence in resonance with these sources.

The microwave field has a complex, frequency dependent mode structure sustained by the experimental set-up. The atom moves through it at a 252±7 m/s velocity. This constraints the timing of the pulses, which can only be applied when the atom is close to an anti-node.

Moreover, the modes have an uncontrolled polarization (see Methods). The mw pulse for the $|50C^-\rangle \rightarrow |52C^-\rangle$ transfer [Fig. 2(a)] can also address the $|52C^+\rangle \rightarrow |50C^+\rangle$ transition (the residual magnetic field being below 10 μT, the Zeemann effect is negligible). In order to avoid this spurious effect, we apply during the mw pulse a non-resonant σ^+ rf dressing, which shifts the $|52C^+\rangle \rightarrow |50C^+\rangle$ transition out of resonance.

Finally, during the preparation sequence, the atom is cast in superpositions of states with very different electric dipoles. It is thus sensitive to the unavoidable electric field noise [6]. We minimize this adverse effect by making the preparation as short as possible and using composite echo pulses (see Methods). The precise sequence timing is described in Fig. 2(b).

We first check the final state populations with a field-ionization detector into which the atom finally reaches after a 225 μs time of flight. The ionization signals are presented in Fig. 3(a). From the heights of the peaks, we infer that we detect on the average 0.63(3) atoms in $|52C^+\rangle$ and 0.47(2) atoms in $|52C^-\rangle$ for each repetition of the sequence. We normalize these signals to the average number of atoms (1.75 ± 0.02) laser-excited in $|52;+2\rangle$

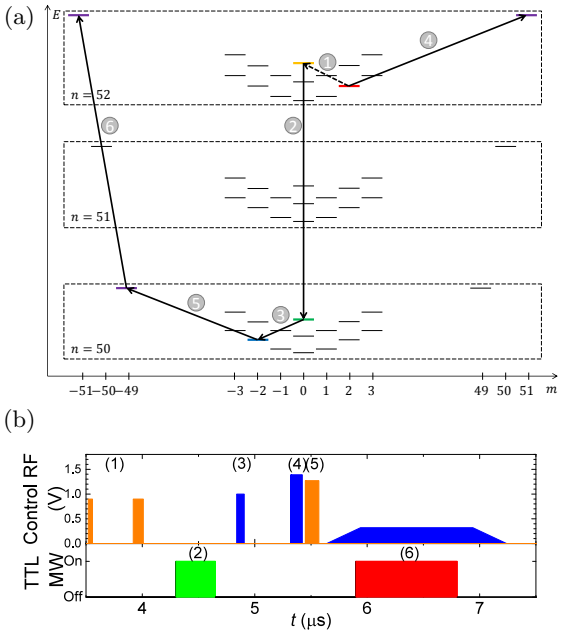

FIG. 2. **Preparation sequence.** (a) Relevant energy levels in the $n = 52$ and $n = 50$ manifolds, sorted by m values. The initial laser-excited level, $|52;+2\rangle$ (in red), is the lowest in the $m = +2$ ladder. We first prepare (dashed line, labelled 1) an equal-weight coherent superposition of $|52;+2\rangle$ with an $m = 0$ state ($|52;0\rangle$, in yellow). We then fully transfer $|52;0\rangle$ into the corresponding state in the 50 manifold, $|50;0\rangle$ (in green), with a two-photon microwave (mw) pulse (2) and into $|50;-2\rangle$ (lower state with $m = -2$ in the 50 manifold, in blue) with a two-photon σ^+ rf pulse (3). We apply a σ^+-rf pulse (4) transferring $|52;+2\rangle$ into $|52C^+\rangle$ and then a σ^--rf pulse (5) to transfer $|50;-2\rangle$ into $|50C^-\rangle$. A final mw pulse (6) transfers $|50C^-\rangle$ into $|52C^-\rangle$. (b) Timing of the preparation sequence. Upper frame: voltage that controls the amplitude of the σ^+ (blue) and σ^- (orange) rf pulses. Lower frame: Transistor-transistor logic (TTL) signal that controls the microwave pulses. The pulses are labelled according to (a). Pulse (1) is implemented as an echo $\pi/2 - \pi$ sequence to reduce sensitivity to electric field noise. Pulses (4) and (5) are double pulses separated by a small time interval to improve their efficiency [28]. Note the σ^+ rf dressing during the mw pulse (6).

(measured using a simple high-efficiency adiabatic transfer towards $|52C^+\rangle$). We thus get nearly equal weights (36 ± 1 % and 27 ± 1 %) of the two circular states $|52C^+\rangle$ and $|52C^-\rangle$. The remaining population ($\approx 37\%$) is lost in intermediate states.

The CSS coherence is then assessed by closing the magnetometer quantum interference. The mw mode structure imposes the timing of the return sequence. After a short delay (2μs), we transfer $|52C^-\rangle$ into $|50C^-\rangle$. We complete the return to $|52;0\rangle$ at $t = 14.1$ μs. The complex Ramsey interferometer sequence is closed by a final two-photon rf pulse applied at $t = 14.8$ μs, mixing again $|52;0\rangle$ and $|52;+2\rangle$. The atom is ideally found in one of these two levels.

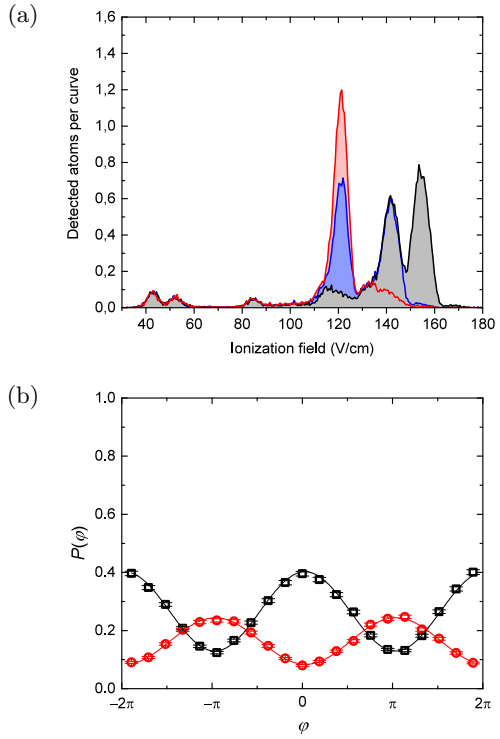

FIG. 3. **Characterization of the CSS.** (a) Field ionization signals. Number of detected electrons per repetition of the experiment as a function of the applied ionization field. The red line corresponds to the final CSS. The blue line is obtained just before the mw pulse (6) performing the $|50C^-\rangle \rightarrow |52C^-\rangle$ transfer. The difference between these two curves (red-shaded area) corresponds to the contribution of the $|52C^-\rangle$ level. Ideally, the corresponding peak of the blue curve measures the $|52C^+\rangle$ population. However, this direct signal is slightly contaminated by a background of spurious high-m levels. In order to estimate this contamination, we record (black line) the ionization signal after transferring $|52C^+\rangle$ into $|49C^+\rangle$. The difference between the blue and black curves (blue shaded zone) gives the background-free contribution of the $|52C^+\rangle$ population. Note that it is a lower estimate due to the finite efficiency of the probe pulse. The small peaks for low fields correspond to spurious populations of low-m levels. (b) Test of the CSS coherence. The black (red) points show the final probability for detecting the atom in the $|52;+2\rangle$ ($|52;0\rangle$) state after closing the interferometer. The errors bars reflect the statistical variance. The lines are sine fits. The difference of the amplitudes of the fringes is due to the limited detection efficiency of $|52;0\rangle$ (see Methods).

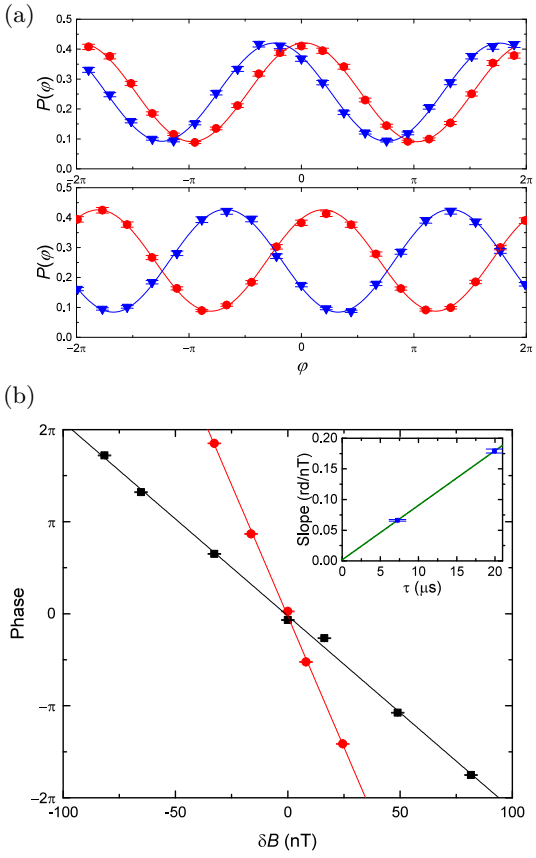

FIG. 4. **Sensitivity to the magnetic field.** (a) Upper frame : Probability for finding the atom in $|52;+2\rangle$ as a function of the interferometer phase φ, for an interrogation time of 7.2 μs, for two applied magnetic fields 0 nT (red points) and 16 nT (blue points). Lower frame: same signals for a 19.9 μs interrogation time and two fields (-16 nT, red, and 0 nT, blue) differing by the same increment as in the upper frame. The errors bars reflect the statistical variance. The lines are sine fits. (b) Phase shift Φ of the interference fringes as a function of the applied magnetic field for a 7.2 μs interrogation time (black dots) and a 19.9 μs one (red dots). The inset gives the slope of these lines as a function of the interrogation time τ. The errors bars reflect the statistical variance of the fit parameters . The slope of the linear fit (blue line) provides the magnetic moment difference of the CSS $[(101 \pm 3)\mu_B]$. Note that the intercept of the fit [0.0018(28) rd/nT] is zero within the error bars. This reflects that the magnetic-field-dependent phase shift accumulated during the preparation and detection sequences of the CSS is negligible.

Fig. 3(b) presents the observed interference pattern. As above, the level populations are normalized to the initial $|52;+2\rangle$ one. We scan the phase φ of the interference by tuning the frequency of the mw inducing the $|52;0\rangle \leftrightarrow |50;0\rangle$ transition. The fringes offset from the ideal 1/2 value shows that about 45% of the population is lost in spurious levels at the end of the complete sequence However, the visibility of the fringes is large (51.2±0.3 %), revealing the coherence of this complex interference process and the preparation of a genuine CSS.

We now test the magnetic field sensitivity of the CSS by applying a small static (< 100 nT) magnetic field $\mathbf{B}$, collinear to $\mathbf{F}$ (see the Methods for the field calibration — note that this small field does not change the tuning of the preparation and detection sequences). In order to make the experiment simpler, with a more flexible timing, we now operate on a CSS $(|52C^+\rangle + |50C^-\rangle)/\sqrt{2}$. It is nearly as sensitive to B as the circular cat and

only marginally more sensitive to the electric field (the differential Stark effect on the levels in this CSS is 535 kHz/(V/cm)^2 only). The mode structure for the remaining mw pulses (on the $|50;0\rangle \leftrightarrow |52;0\rangle$ transition) allows us to use two interrogation time $\tau = \tau_1 = 7.2$ μs and $\tau = \tau_2 = 19.9$ μs (see Methods).

Fig. 4(a) presents the Ramsey fringes for two fields B differing by 16 nT and for the two τ values. As expected, the visibility of the fringes [63.7(2)% for τ_1 and 67.2(3)% for τ_2] is better than in Fig. 3(b) (we avoid the imperfections of the $|50C^-\rangle \leftrightarrow |52C^-\rangle$ transfers). More interestingly, the visibility is about the same for the two τ values, showing that the decoherence time of the CSS is much longer than 20 μs, a promising result. The phase shift due to the field increment is conspicuous in Fig. 4(a).

Fig. 4(b) shows the fringes phase shift Φ as a function of B for the two τ values. The inset shows the slopes of these $\Phi(B)$ lines [0.179(3) and 0.066(1) rd/nT] as the function of the interrogation time. From the difference of these slopes, we deduce an effective CSS magnetic moment of 101(3) μ_B, in fair agreement with the expected value (100 μ_B). This brings another evidence that we indeed reach the target CSS.

We assess the sensitivity with the classical Fisher information, $\mathcal{F}$, deduced from the measurement of the final populations at mid-fringe ($\varphi = \Phi + \pi/2$; highest sensitivity, see Methods). We infer, for $\tau = \tau_2$, a Cramér-Rao limit for the single-atom sensitivity of 13.2(2) nT. This corresponds to the sensitivity that we would obtain with an ideal measurement on $N \approx 1800$ independent atoms using a transition with one μ_B magnetic moment difference [24]. This number N would reach 10 000 in an ideal experiment with a unity fringes contrast. It scales moreover as the square of the principal quantum number.

Our scheme could be considerably improved. Modulating the envelope of the rf pulses should allow reaching higher preparation and read-out efficiencies [28]. Using slow, and eventually trapped Rydberg atoms [29], will overcome the limitation due to the transit through the mw mode structure. The magnetic field sensitivity would then be limited by the intrinsic spontaneous emission lifetime of the CSS (30 ms). It would reach 700 fT/$\sqrt{\text{Hz}}$, beating the best single-particle (single-ion) magnetometers so far, with 4 pT/$\sqrt{\text{Hz}}$ sensitivity[20, 25]. Spontaneous emission inhibition [30] could even lead to much longer interrogation times, in the second range [29], leading to unprecedented sensitivities. Finally the method is not limited to $n \approx 50$ and could be transposed to manifolds with higher ns. There is thus a bright future for local probes of the magnetic fields based on circular state quantum superpositions.

Acknowledgements : We thank Ch. Koch and S. Patsch for extremely useful discussions. We acknowledge financial support by the European Union under the Research and Innovation action project "RYSQ" (640378) and by the Agence Nationale de la Recherche under the project "SNOCAR" (167754).

Author Contributions: E.K.D and A.L contributed equally. E.K.D, A.L., J.M.R, S.H, M.B. and S.G. contributed to the experimental set-up. E.K.D and A.L collected the data and analysed the results. S.G. supervised the experiment. All authors discussed the results and the manuscript.

Author Information: The authors declare no competing financial interests.

Data availability : The data that support the plots within this paper and other findings of this study are available from the corresponding author upon reasonable request.

* gleyzes@lkb.ens.fr

[1] Markus Greiner, Olaf Mandel, Theodor W. Hänsch and Immanuel Bloch Collapse and revival of the matter wave field of a BoseEinstein condensate *Nature*, 519, 51–54, 2002.

[2] Jean-Michel Raimond and Serge Haroche. Exploring the quantum *Oxford Graduate Texts*, 2006.

[3] Samuel Deléglise, Igor Dotsenko, Clment Sayrin, Julien Bernu, Michel Brune, Jean-Michel Raimond, and Serge Haroche. Reconstruction of non-classical cavity field states with snapshots of their decoherence. *Nature*, 455(7212):510–514, September 2008.

[4] Chen Wang, Yvonne Y Gao, Philip Reinhold, Reinier W Heeres, Nissim Ofek, Kevin Chou, Christopher Axline, Matthew Reagor, Jacob Blumoff, KM Sliwa, et al. A schrödinger cat living in two boxes. *Science*, 352(6289):1087–1091, 2016.

[5] K.G. Johnson, J.D Wong-Campos, B. Neyenhuis, J. Mizrahi and C. Monroe Ultrafast creation of large Schrödinger cat states of an atom *Nature communications*, 8(1):697, 2017.

[6] Adrien Facon, Eva-Katharina Dietsche, Dorian Grosso, Serge Haroche, Jean-Michel Raimond, Michel Brune, and Sébastien Gleyzes. A sensitive electrometer based on a rydberg atom in a schrödinger-cat state. *Nature*, 535(7611):262–265, 07 2016.

[7] Pavel Ripka. Review of fluxgate sensors. *Sensors and Actuators A: Physical*, 33, 129–141, 1992.

[8] Matti Hämäläinen, Riitta Hari, Risto J Ilmoniemi, Jukka Knuutila, and Olli V Lounasmaa. Magnetoencephalographytheory, instrumentation, and applications to noninvasive studies of the working human brain. *Reviews of modern Physics*, 65(2), 413 – 497, 1993.

[9] TH Sander, J Preusser, R Mhaskar, J Kitching, L Trahms, and S Knappe. Magnetoencephalography with a chip-scale atomic magnetometer. *Biomedical optics express*, 3(5):981–990, 2012.

[10] D Le Sage, K Arai, DR Glenn, SJ DeVience, LM Pham, L Rahn-Lee, MD Lukin, A Yacoby, A Komeili, and RL Walsworth. Optical magnetic imaging of living cells. *Nature*, 496(7446):486–489, 2013.

[11] Kasper Jensen, Rima Budvytyte, Rodrigo A Thomas, Tian Wang, Annette M Fuchs, Mikhail V Balabas, Georgios Vasilakis, Lars D Mosgaard, Hans C Stærkind, Jörg H Müller, et al. Non-invasive detection of animal nerve impulses with an atomic magnetometer operating near quantum limited sensitivity. *Scientific reports*, 6:29638, 2016.

[12] SJ Swithenby. Squids and their applications in the measurement of weak magnetic fields. *Journal of Physics E: Scientific Instruments*, 13(8):801 –813, 1980.

[13] IK Kominis, TW Kornack, JC Allred, and MV Romalis. A subfemtotesla multichannel atomic magnetometer. *Nature*, 422(6932):596-599, 2003.

[14] W. Wasilewski, K. Jensen, H. Krauter, J. J. Renema, M. V. Balabas, and E. S. Polzik. Quantum noise limited and entanglement-assisted magnetometry. *Phys. Rev. Lett.*, 104:133601, Mar 2010.

[15] Mustafa Bal, Chunqing Deng, Jean-Luc Orgiazzi, FR Ong, and Adrian Lupascu. Ultrasensitive magnetic field detection using a single artificial atom. *Nature communications*, 3:1324, 2012.

[16] Stephan Wildermuth, Sebastian Hofferberth, Igor Lesanovsky, Elmar Haller, L Mauritz Andersson, Sönke Groth, Israel Bar-Joseph, Peter Krüger, and Jörg Schmiedmayer. Bose–einstein condensates: Microscopic magnetic-field imaging. *Nature*, 435(7041):440, 2005.

[17] M Vengalattore, JM Higbie, SR Leslie, J Guzman, LE Sadler, and DM Stamper-Kurn. High-resolution magnetometry with a spinor bose-einstein condensate. *Physical review letters*, 98(20):200801, 2007.

[18] Caspar F. Ockeloen, Roman Schmied, Max F. Riedel, and Philipp Treutlein. Quantum metrology with a scanning probe atom interferometer. *Phys. Rev. Lett.*, 111:143001, Oct 2013.

[19] Wolfgang Müssel, H Strobel, D Linnemann, DB Hume, and MK Oberthaler. Scalable spin squeezing for quantum-enhanced magnetometry with bose-einstein condensates. *Phys. Rev. Lett.*, 113(10):103004, 2014.

[20] T Ruster, H Kaufmann, MA Luda, V Kaushal, CT Schmiegelow, F Schmidt-Kaler, and UG Poschinger. Entanglement-based dc magnetometry with separated ions. *Physical Review X*, 7(3):031050, 2017.

[21] JM Taylor, P Cappellaro, L Childress, L Jiang, D Budker, PR Hemmer, A Yacoby, R Walsworth, and MD Lukin. High-sensitivity diamond magnetometer with nanoscale resolution. *Nature Physics*, 4(10):810–816, 2008.

[22] Gopalakrishnan Balasubramanian, IY Chan, Roman Kolesov, Mohannad Al-Hmoud, Julia Tisler, Chang Shin, Changdong Kim, Aleksander Wojcik, Philip R Hemmer, Anke Krueger, et al. Nanoscale imaging magnetometry with diamond spins under ambient conditions. *Nature*, 455(7213):648–651, 2008.

[23] JR Maze, PL Stanwix, JS Hodges, S Hong, JM Taylor, P Cappellaro, L Jiang, MV Gurudev Dutt, E Togan, AS Zibrov, et al. Nanoscale magnetic sensing with an individual electronic spin in diamond. *Nature*, 455(7213):644–647, 2008.

[24] Robert Maiwald, Dietrich Leibfried, Joe Britton, James C Bergquist, Gerd Leuchs, and David J Wineland. Stylus ion trap for enhanced access and sensing. *Nature Physics*, 5(8):551–554, 2009.

[25] I. Baumgart, J.-M. Cai, A. Retzker, M. B. Plenio, and Ch. Wunderlich. Ultrasensitive magnetometer using a single atom. *Phys. Rev. Lett.*, 116:240801, Jun 2016.

[26] Thomas Chalopin, Chayma Bouazza, Alexandre Evrard, Vasiliy Makhalov, Davide Dreon, Jean Dalibard, Leonid A Sidorenkov, and Sylvain Nascimbene. Quantum-enhanced sensing using non-classical spin states of a highly magnetic atom. *Nat. Commun.*, 9:4955, 2018.

[27] A. Signoles, E. K. Dietsche, A. Facon, D. Grosso, S. Haroche, J. M. Raimond, M. Brune, and S. Gleyzes. Coherent transfer between low-angular-momentum and circular rydberg states. *Phys. Rev. Lett.*, 118:253603, Jun 2017.

[28] Sabrina Patsch, Daniel M. Reich, Jean-Michel Raimond, Michel Brune, Sébastien Gleyzes, and Christiane P. Koch. Fast and accurate circularization of a rydberg atom. *Phys. Rev. A*, 97:053418, May 2018.

[29] T. L. Nguyen, J. M. Raimond, C. Sayrin, R. Cortiñas, T. Cantat-Moltrecht, F. Assemat, I. Dotsenko, S. Gleyzes, S. Haroche, G. Roux, Th. Jolicoeur, and M. Brune. Towards quantum simulation with

circular rydberg atoms. *Phys. Rev. X*, 8:011032, 2018.

[30] D. Hanneke, S. Fogwell Hoogerheide, and G. Gabrielse. Cavity control of a single-electron quantum cyclotron: Measuring the electron magnetic moment. *Phys. Rev. A*, 83:052122, May 2011.

METHODS

Experimental apparatus

The setup is made up of two parallel, horizontal disk electrodes, which create the vertical electric field F aligned along the Oz axis. The gap between them is surrounded by four other electrodes forming a ring, used to generate the $\sigma^{\pm}$ polarized rf fields (see supplementary information, Fig. S1).

The Rydberg atoms are excited stepwise by three laser beams at 780 nm, 776 nm and 1258 nm resonant with the $5S_{1/2} \rightarrow 5P_{3/2}$, $5P_{3/2} \rightarrow 5D_{5/2}$ and $5D_{5/2} \rightarrow 52F$ transitions respectively. In the horizontal plane, they cross at a 45° angle the horizontal atomic beam at the center of the electrode structure. The Doppler effect provides an atomic velocity selection at $v = 252 \pm 7$ m/s. The 780 and 776 nm cw laser beams are collinear, perpendicular to the 1258 nm one. The latter is pulsed. The beginning of this 1 μs-long pulse sets the time origin, $t = 0$, of the experimental sequence.

The quantization axis during the laser excitation is parallel to the σ^+-polarized 780 and 776 nm laser beams (the 1258 nm beam is π-polarized with respect to this axis). It is defined by dc potentials applied across the ring electrodes. Between $t = 2$ μs and $t = 3$ μs, this horizontal field is adiabatically switched off, while we switch on an electric field aligned with Oz, which becomes the quantization axis for the rest of the experiment. The choice of laser polarizations and the quantization axis adiabatic evolution result in the selective preparation of $|52; +2\rangle$.

We control the polarization of the rf generated at the center of the structure by adjusting the phase and amplitude (using frequency mixers driven by a control voltage) of the synthesizers connected to the four ring electrodes. This optimization is performed at a fixed frequency. We use two sets of rf synthesizers. The first generates a σ^+ rf field at $\omega^+/2\pi = 230$ MHz. The second generates a σ^- rf field at $\omega^-/2\pi = 221.64$ MHz. The chosen frequencies optimize the efficiency of the rf transfer from $|52; +2\rangle$ to $|52C^+\rangle$ and from $|50; -2\rangle$ to $|50C^-\rangle$ respectively for $F = F_0$.

The microwave fields are fed through a waveguide placed outside the electrodes. This waveguide couples to the microwave eigenmodes of the structure. The amplitude (and the polarization) of the microwave field pulses experienced by the atoms depends thus on their position at the time t of the pulse. For the π-polarized component of the microwave at the frequency of the $|52; 0\rangle \leftrightarrow |50; 0\rangle$ two-photon transition we observe only two anti-nodes between $6 \leq t \leq 32$ μs, centered around $t = 14.2$ μs and $t = 26.6$ μs (see supplementary information, Fig S2). This limits the possible interrogation times for the magnetometer to two narrow intervals around the τ_1 and τ_2 values given in the main text.

Calibration of the magnetic field

The magnetic field increment δB is applied using two coils surrounding the experimental set-up. The increment δB is calibrated against the current I in the coils by recording Ramsey fringes on the $|52C^+\rangle \leftrightarrow |50C^+\rangle$ two-photon transition. We apply two $\pi/2$ pulses at $t = 7.2$ μs and $t = 27.2$ μs and record the probability to detect the atom in $|52C^+\rangle$ as a function of the relative phase of the pulses, using large I values to get a sensible fringes phase shift in spite of the low magnetic dipole difference ($2\mu_B$) of the levels. We obtain $\partial B/\partial I = 21.2 \pm 0.2$ nT/mA.

Description of the $m \geq 2$ Rydberg levels in terms of an effective angular momentum

The energy structure of the Rydberg levels of rubidium is given by the Stark map depicted in Fig. 1 (and supplementary information Fig. S3). Since the field preserves a cylindrical symmetry around Oz, m remains a good quantum number and the levels can be sorted as a function of m. The transitions between adjacent m states are coupled to a well-defined polarization of the electromagnetic field. A rf field with σ^+ polarization, for instance, couples only to transitions along an up-right diagonal.

If the atom is initially in the $|52, +2\rangle$ state, a σ^+ rf field at frequency $\omega^+_{rf}/2\pi$ couples it only to the levels of the lower diagonal on the right of the energy structure (see supplementary information, Fig. S3). The dynamics inside this set of levels is (to first order in F) that of an angular momentum $\mathbf{J}^+_{52}$ with $J^+_{52} = 51/2$. Each state $|52, m\rangle$ of this lower diagonal corresponds to the state $|m_{J^+_{52}} = -51/2 + m\rangle$ of the angular momentum (the levels $m_{J^+_{52}} = -51/2$ and $m_{J^+_{52}} = -49/2$ are missing due to the quantum defect perturbation) [26]. The evolution is given by the Hamiltonian

$$H_{J^+_{52}} = \hbar\Delta J^+_{52,z} + \hbar\Omega^+_{52} J^+_{52,x}$$

where $\Delta = \omega_S(52) - \omega^+_{rf}$ and $\Omega^+_{52} = 3nea_0F^+_{rf}/2\hbar$ is proportional to the amplitude F^+_{rf} of the σ^+ rf field.

Similarly, an atom initially in $|52C^+\rangle$ is coupled by a σ^- rf field to the upper right diagonal of the energy structure. The dynamics is that of an effective angular momentum $\mathbf{J}^-_{52}$, with $J^-_{52} = 51/2$. The m levels of the upper diagonal correspond to the states $|m_{J^-_{52}} = 51/2 - m\rangle$ of $\mathbf{J}^-_{52}$. The circular state is the level with $m_{J^-_{52}} = -51/2$.

Experimental sequence

The preparation of the circular cat state from $|52;+2\rangle$ involves a series of rf and mw pulses.

We start with a static electric field of 1.39 V/cm, chosen so that the 221.64 MHz σ^--polarized rf field is resonant with the two-photon $|52;+2\rangle \leftrightarrow |52;0\rangle$ transition. We prepare the superposition $1/\sqrt{2}(|52;+2\rangle + |52;0\rangle)$ in two steps : first we apply at $t = 1.88$ μs a 38 ns $\pi/2$ pulse that prepares a superposition of the two states. It is followed at $t = 2.28$ μs by a 90 ns π pulse that swaps $|52;+2\rangle$ and $|52;0\rangle$. This echo pulse limits the sensitivity of the cat state preparation process to the electric field noise (see below). For these two pulses, the rf detuning with respect to the transition toward the intermediate state $|52;+1\rangle$ (≈ 43 MHz) is not much larger than the Rabi frequency (~ 25 MHz). As a result, $|52;+1\rangle$ is transiently populated during the rf pulse. However its population periodically returns to zero in the non-resonant Rabi oscillation process. We precisely tune the pulse durations so that no appreciable population is finally left in $|52;+1\rangle$ (see supplementary information, Fig. S4).

We then ramp up the electric field to 1.48 V/cm, and apply at $t = 4.3$ μs a 0.35 μs microwave π pulse at 49.368 GHz that transfers $|52;0\rangle$ into $|50;0\rangle$ with a $82.5 \pm 0.6\%$ efficiency.

We increase further the electric field to 1.50 V/cm, bringing the $|50;0\rangle \leftrightarrow |50;-2\rangle$ two-photon transition on resonance with the 230 MHz σ^+-polarized rf field for a π pulse. The choice of the rf pulse duration takes into account two effects. First, as above, the detuning Δ_{-1} to the intermediate state $|50;-1\rangle$ is not much larger than the rf-induced Rabi frequency. The population of $|50;-1\rangle$ oscillates with a period T_{-1}. Second, the Stark frequency ω_s in the $n = 52$ manifold at this electric field is 150 MHz. The σ^+-polarized rf field is thus detuned by only $\Delta_{52} = 80$ MHz from the transition between the hydrogenic ladder states $|52;m \geq 2\rangle$. The rf thus induces an oscillation of the $|52;+2\rangle$ population with a period T_{52}. To ensure that $|50;-1\rangle$ is not populated and, simultaneously, that $|52;+2\rangle$ is not affected, we choose a duration for the rf pulse (66 ns) close to an integer number of T_{-1} and T_{52} (see supplementary information, Fig. S5).

We then increase the electric field further to $F = F_0$ to perform the transfers into the circular states. We first apply the σ^+-polarized rf field transferring $|52;+2\rangle$ into $|52C^+\rangle$. Instead of a single fixed amplitude rf pulse, we program a 5 ns pulse followed 3 ns later by a 95 ns one. This rf drive pulse modulation (inspired by [28]) slightly increases the transfer efficiency towards the circular state by reducing the population off-resonantly transferred into the $m = 1$ state below $|52;+2\rangle$ (see supplementary information, Fig. S6).

The state $|50;-2\rangle$ is unaffected by these σ^+-polarized rf pulses, as all σ^+ transitions from $|50;-2\rangle$ are far-detuned from 230 MHz. About 30 ns after the end of the σ^+ pulses, we apply two 221.64 MHz σ^- rf pulses (4 ns and 112 ns separated by 4 ns) to transfer $|50;-2\rangle$ into $|50C^-\rangle$. This σ^- rf field affects the part of the wavefunction in $|52C^+\rangle$, since it couples this state to the levels of the upper right diagonal of the Stark manifold. This dynamics is described by the angular momentum $\mathbf{J}^-_{52}$, rotating under the action of the non-resonant σ^- rf field. The population thus periodically comes back into $|52C^+\rangle$. We choose the power and duration of the σ^--polarized rf field double-pulse to optimize the $|50;-2\rangle$ to $|50C^-\rangle$ transfer while inducing exactly a 2π rotation of $\mathbf{J}^-_{52}$.

At this point, the atom is ideally in the superposition $1/\sqrt{2}(|52C^+\rangle + |50C^-\rangle)$. To prepare the circular cat, we finally transfer $|50C^-\rangle$ into $|52C^-\rangle$. However, the transitions $|50C^+\rangle \leftrightarrow |52C^+\rangle$ and $|50C^-\rangle \leftrightarrow |52C^-\rangle$ are at the same frequency. In order to transfer $|50C^-\rangle$ into $|52C^-\rangle$ without transferring $|52C^+\rangle$ into $|50C^+\rangle$, we apply a σ^+-polarized rf field that light-shifts in opposite directions circular states with opposite angular momenta.

To that end, at $t = 5.7$ μs, we increase the amplitude of the electric field by 0.05 V/cm. This field increment shifts the Stark frequencies ω_{52} and ω_{50} by ~ 5 MHz. In the meantime, we apply a small σ^+-polarized rf field, with a Rabi frequency $\Omega^+_{52}/2\pi \approx 0.4$ MHz. This rf field is switched on slowly enough (in 300 ns) so that the atom adiabatically evolves into a superposition of the rf-dressed eigenstates $|52C^+\rangle^*$ and $|50C^-\rangle^*$, which are both light-shifted to higher energies. On the contrary, the rf-dressed states $|52C^-\rangle^*$ and $|50C^+\rangle^*$ are shifted to lower energies. As a result, the two photon $|50C^-\rangle^* \leftrightarrow |52C^-\rangle^*$ transition is red-shifted by ~ 1 MHz, while the $|50C^+\rangle^* \leftrightarrow |52C^+\rangle^*$ transition is blue shifted by approximatively the same amount. This allows us to transfer $|50C^-\rangle^*$ into $|52C^-\rangle^*$ by a 0.9 μs pulse at $t = 5.9$ μs without affecting $|52C^+\rangle^*$. We then ramp down the rf field in 300 ns to adiabatically transfer the superposition $1/\sqrt{2}(|52C^+\rangle^* + |52C^-\rangle^*)$ into $1/\sqrt{2}(|52C^+\rangle + |52C^-\rangle)$ (see supplementary information, Fig. S7).

We test the coherence of the superposition by reversing the full process. The structure of the microwave mode at the $50C \leftrightarrow 52C$ frequency is such that the amplitude of the σ^- component starts to decrease after $t = 8$ μs. Consequently, 200 ns after switching off the σ^+ rf dressing, we switch it back on in 300 ns, and apply at $t = 7.7$ μs a 0.9 μs π-pulse that selectively transfers $|52C^-\rangle^*$ back into $|50C^-\rangle^*$.

For the $|50;0\rangle \leftrightarrow |52;0\rangle$ transition, we can use two antinodes along the trajectory of the atoms. We can apply the return $|50;0\rangle \leftrightarrow |52;0\rangle$ π pulse either at $t_1 = 13.8$ μs or at $t_2 = 26.5$ μs. In order to reduce the decoherence induced by the electric field noise, we leave as long as possible the atom in $1/\sqrt{2}(|52C^+\rangle + |50C^-\rangle)$, which is nearly

insensitive to the electric field. We start the remaining time-reversed sequence 1 μs before t_i (the durations and delays of each microwave or rf pulse have been re-optimized independently from the direct sequence). Finally, we close the interference process by a final $\pi/2$ pulse on the $|52;0\rangle \leftrightarrow |52;0\rangle$ transition.

Assessment of the prepared state

The atom are detected by state-selective field ionization in a detector outside the electrode structure. Among all levels of interest, the detector resolves Rydberg levels with similar ms and different principal quantum numbers n. However, levels with the same n, which only differ by a few units in m have very similar ionization thresholds and cannot be resolved. To assess the population of a single target Stark level, we used two different methods.

Probe pulses. We apply a π microwave "probe" pulse that selectively transfers the population of the target level into a different manifold. We measure how many atoms are detected in the initial manifold with and without the transfer probe pulse. Assuming a perfect π pulse, the missing atoms correspond to the population of the target state. In practice, the microwave pulse is not perfect, and this measurement provides a lower bound on the target state population. We use this method to measure the number of atoms in $|52C^+\rangle$ or $|52C^-\rangle$.

Adiabatic transfer The coherence of the circular cat state is probed by measuring the population of $|52;2\rangle$ and $|52;0\rangle$ after the final $\pi/2$ pulse. Since these two states have nearly the same ionization threshold, shortly after the $\pi/2$ pulse, we adiabatically transfer with a nearly 100% efficiency $|52;2\rangle$ into $|52C^+\rangle$ with a rf pulse [26]. This pulse does not affect $|52;0\rangle$, due to the anharmonicity of the level structure for low-m states. The atoms detected at the low-m ionization threshold correspond to the $|52;0\rangle$ population, and those detected at the $|52C^+\rangle$ threshold correspond to $|52;2\rangle$.

The measured detection efficiency ratio between $|52;2\rangle$ and $|52;0\rangle$ is 1.77 ± 0.05. Its departure from unity is mainly due to the spontaneous decay of $|52;0\rangle$ during the 225 μs time-of-flight between the center of the electrodes and the detector.

Optimizing the CSS insensitivity to electric field

The circular cat superposition is totally insensitive to the electric field noise, as $|52C^-\rangle$ and $|52C^+\rangle$ experience by symmetry the same Stark effect. However, during the preparation sequence, the atom is transiently cast in superpositions of states with very different electric dipoles. The electric field noise thus induces a random differential phase between the two arms of the Ramsey interferometer. We use two different strategies to limit this adverse effect.

Echo π pulse. The level $|52;2\rangle$ has a larger electric dipole than $|52;0\rangle$, $|50;0\rangle$ or $|50;-2\rangle$. As a result, the two arms of the quantum interferometer corresponding to $|52;2\rangle$ and $|52;0\rangle$ immediately after the $\pi/2$ pulse accumulate a field-sensitive relative phase. In order to limit the contrast reduction due to the electric field noise, we apply after 362 ns a π pulse exchanging the two arms of the interferometer. The relative phase shift due to the electric field noise accumulated before the π pulse compensates that acquired after the π pulse. Similarly, we apply a π pulse before the final $\pi/2$ pulse of the sequence in order to limit the decoherence induced by the electric field noise at the end of the reverse sequence.

Order of the circularization pulses. We also limit the effect of decoherence by transferring $|52;2\rangle$ into $|52C^+\rangle$ before transferring $|50;-2\rangle$ into $|50C^-\rangle$. Since $|52C^+\rangle$ has nearly no permanent electric dipole, the relative phase accumulated when the atom is in a superposition $1/\sqrt{2}(|52C^+\rangle + |50;-2\rangle)$ cancels the phase accumulated when the atom was in $1/\sqrt{2}(|52,2\rangle + |50;-2\rangle)$ (see supplementary information for additional information).

Phase measurements and Fisher information

The single-atom sensitivity σ_B^1 of the magnetic field measurement is given by the Cramér-Rao bound

$$\sigma_B^1 = 1/\sqrt{\mathcal{F}_B}$$

where $\mathcal{F}_B$ is the Fisher information

$$\mathcal{F}_B = \sum_i \frac{(\partial P_i/\partial B)^2}{P_i}$$

The index i enumerate the outcomes of the measurement. We can rewrite $\mathcal{F}_B = (\partial\Phi/\partial B)^2\mathcal{F}_\Phi$, with

$$\mathcal{F}_\Phi = \sum_i \frac{(\partial P_i/\partial \Phi)^2}{P_i}.$$

Ideally, the atom exits the interferometer in either $|52;0\rangle$ or $|52;+2\rangle$, and we would observe, as a function of the Ramsey phase, sine fringes with a perfect contrast. The Fisher information $\mathcal{F}_\Phi$ would then be equal to 1, leading to a sensitivity

$$\sigma_B^{1,ideal} = \left(\frac{\partial\Phi}{\partial B}\right)^{-1} = \frac{\hbar}{100\mu_B\tau}\ .$$

Experimentally, part of the atomic population is lost in intermediate levels, $|52;0\rangle$ has a limited detection efficiency and the fringes visibility is lower than one. We must thus to consider three different outcomes i : (a) the atom is detected in $|52;2\rangle$, (b) the atom is detected in $|52;0\rangle$, and (c) the atom is not detected at all (either it is lost in an intermediate level, or it was in $|52;0\rangle$

but decayed by spontaneous emission). The probabilities $P_a(\Phi)$, $P_b(\Phi)$ and $P_c(\Phi)$ are given by

$$P_a(\Phi) = \bar{P}_2 + \frac{C_2}{2}\cos(\Phi - \varphi)$$
$$P_b(\Phi) = \bar{P}_0 - \frac{C_0}{2}\cos(\Phi - \varphi)$$
$$P_c(\Phi) = 1 - P_a(\Phi) - P_b(\Phi)$$

The optimum sensitivity is obtained for $\varphi = \Phi + \pi/2$. From the fits to the experimental data for an interrogation time $\tau = \tau_2$, we find $C_2 = 0.343$, $C_0 = 0.198$, $\bar{P}_2 = 0.256$ and $\bar{P}_0 = 0.179$, so that $(\mathcal{F}_\Phi)^{1/2} = 0.42$. Combining this value with the phase sensitivity $(\partial\Phi/\partial B) = 0.179(3)$ rd/nT (Fig. 4), we get a single atom sensitivity $\sigma_B^1 = 13.2 \pm 0.2$ nT.